

Design and Performance Simulation of the Electromagnetic Calorimeter at EicC

Ye Tian,^{a,1} Souvik Maity,^a Jingyu Li,^a Yuancai Wu,^{a,b} Shan Sha,^a Yutie Liang,^{a,b,c}
Aiqiang Guo,^{a,b,c} Yuxiang Zhao,^{a,b,c} and Dexu Lin^{a,b,c,1}

^a*Institute of Modern Physics, Chinese Academy of Sciences, Lanzhou, Gansu Province 730000, China*

^b*School of Nuclear Science and Technology, University of Chinese Academy of Sciences, Beijing 100049, China*

^c*Heavy Ion Science and Technology Key Laboratory, Institute of Modern Physics, Chinese Academy of Sciences, Lanzhou 730000, China,*

E-mail: tianye@impcas.ac.cn, dxlin@impcas.ac.cn

ABSTRACT: The Electromagnetic Calorimeter (ECAL) is a key detector component for precise measurements of electrons and photons in electron–ion collision experiments. At the Electron–Ion Collider in China (EicC), high-performance calorimetry is essential for exploring the internal structure of nucleons and studying the dynamics of quarks and gluons within quantum chromodynamics (QCD). This paper presents the optimized design and performance simulation of the EicC ECAL system. The ECAL consists of three specialized sections tailored to distinct detection environments: (1) an electron-Endcap employing high-resolution pure Cesium Iodide (pCsI) crystals, (2) a central barrel, and (3) an ion-Endcap, both adopting a cost-effective Shashlik-style sampling calorimeter with improved light yield. Each segment’s geometry and material composition have been systematically optimized through Geant4 simulations to achieve excellent energy and position resolutions as well as strong electron–pion discrimination. The simulated performance indicates that the ECAL can achieve energy resolutions of $1.76\%/ \sqrt{E(\text{GeV})} \oplus 1.53\%$ for pCsI crystals and $5\%/ \sqrt{E(\text{GeV})} \oplus 4.2\%$ for Shashlik modules, meeting the design goals of the EicC detector.

KEYWORDS: Electromagnetic Calorimeter, Sampling Calorimeter, Homogeneous Calorimeter, Monte Carlo Simulation, Reconstruction

¹Corresponding author.

Contents

1	Introduction	1
2	Electromagnetic Calorimeter Design	3
2.1	CsI Module Design	4
2.2	Shashlik Module Design	6
3	Simulation Results and Detector Design Optimization	7
3.1	Energy Reconstruction and Resolution	8
3.2	Position Reconstruction and Resolution	8
3.3	Electron and Pion Identification	9
3.4	Design Optimization	12
4	Neutral Pion Reconstruction	13
5	Conclusions	15

1 Introduction

The Electron–Ion Collider in China (EicC) [1], proposed as a new facility at the High Intensity Heavy-ion Accelerator Facility (HIAF) [2] in Huizhou, is designed to advance our understanding of quantum chromodynamics (QCD). Through high-energy electron–ion collisions, it will probe the internal structure of nucleons, with particular emphasis on the origins of nucleon spin and mass, the dynamics of quarks and gluons, and the fundamental properties of the strong interaction.

A schematic view of the EicC spectrometer is shown on the left of Fig. 1. The detector provides nearly 4π coverage for scattered particles. Fig. 2 shows the momentum and pseudorapidity distributions of scattered electrons and π^0 mesons, while Fig. 3 presents the corresponding π/e ratio. All figures are obtained from ep scattering events generated with PYTHIA [3], assuming 3.5 GeV electrons colliding with 20 GeV protons. The broad kinematic distributions highlight the need for uniform and high-resolution calorimetry across a wide angular range. The expected luminosity is $L = 4 \times 10^{33} \text{ cm}^{-2}\text{s}^{-1}$, corresponding to an interaction rate of approximately 83.2 kHz, with an average final-state particle multiplicity of about 9 per event.

Due to the asymmetric beam energies at the EicC, the ECAL must operate effectively across a wide and region-dependent dynamic range. The ECAL is responsible for detecting electrons and photons within the pseudorapidity range $|\eta| < 3$, which corresponds to approximately 99% of the total solid angle. To achieve the required performance across this coverage, the ECAL is divided into three segments: the electron-endcap (e-Endcap), the central barrel, and the ion-Endcap. Each segment adopts a calorimeter technology optimized for its specific physics and geometrical constraints.

The main performance requirements of the ECAL are as follows:

- Efficient reconstruction of scattered electrons and reliable separation from the pion background.
- Accurate reconstruction of photons with excellent energy and position resolutions.
- Capability to reconstruct high-energy π^0 mesons from their two-photon decays.

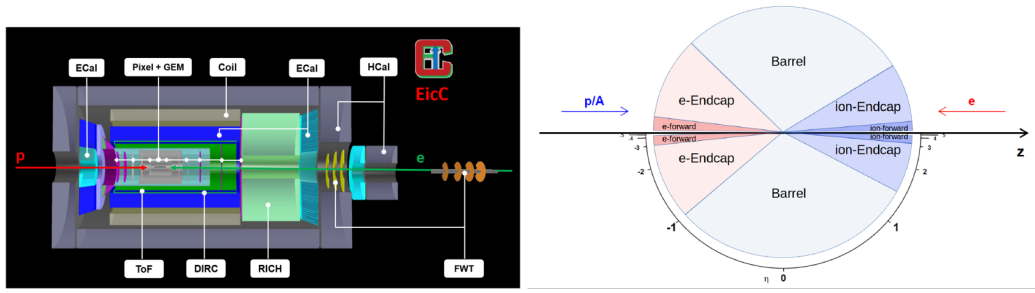


Figure 1. The EicC spectrometer design (left) and the coordinate definition of the detector segment (right) [1].

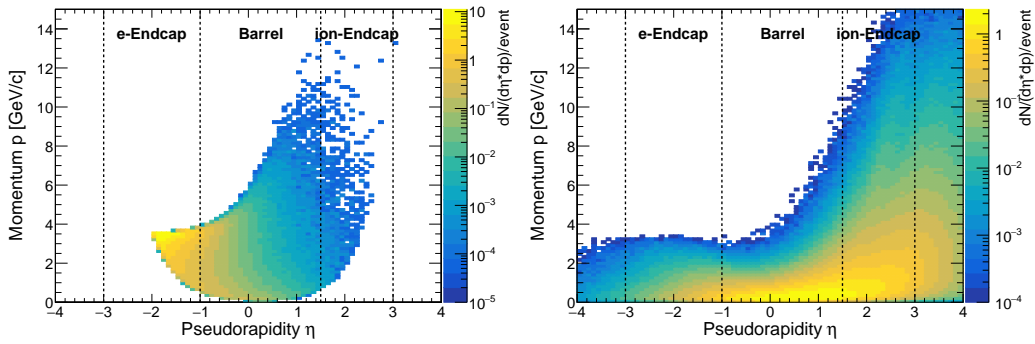


Figure 2. Momentum and pseudorapidity distributions of scattered electrons (left) and neutral pions (right) from EicC ep scattering events. The data are obtained from Pythia simulations of 3.5 GeV electrons colliding with 20 GeV protons, with a kinematic requirement of $Q^2 > 1 \text{ GeV}^2$ applied.

To meet these goals, the e-Endcap employs a high-resolution pure CsI (pCsI) crystal calorimeter, targeting an energy resolution better than $2.5\%/\sqrt{E(\text{GeV})}$ for electrons up to 4 GeV. The barrel and ion-Endcap regions utilize a Shashlik-style sampling calorimeter, optimized for light yield and uniformity, with an energy resolution of about $5\%/\sqrt{E(\text{GeV})}$ for photons and electrons up to 15 GeV. A position resolution better than $6 \text{ mm}/\sqrt{E(\text{GeV})}$ and a timing precision below 1 ns are also required to suppress pile-up and improve particle identification.

Careful consideration has therefore been devoted to the design and optimization of each calorimeter segment. A combination of homogeneous crystal and sampling technologies provides a balanced solution between energy resolution, particle identification (PID), and cost, ensuring that the ECAL can fully support the precision physics program of the EicC.

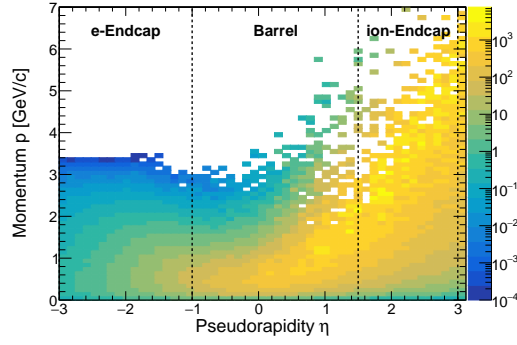


Figure 3. The π/e ratio as a function of momentum and pseudorapidity is obtained from EicC ep scattering events. The electrons are composed of scattered electrons and secondary electrons originating from e^+e^- pair production. To evaluate the impact of pion background, in contrast to Fig. 2, no kinematic requirement of $Q^2 > 1 \text{ GeV}^2$ is applied in this case.

2 Electromagnetic Calorimeter Design

Based on the detection requirements across different kinematic regions at EicC, the e-Endcap, barrel, and ion-Endcap sections of the ECAL are configured to cover pseudorapidity intervals of $(-3, -1)$, $(-1, 1.5)$, and $(1.5, 3)$, respectively. The segments and corresponding coverages are illustrated in Fig. 1. The e-Endcap is designed for precise detection of scattered electrons, utilizing a homogeneous crystal calorimeter with excellent energy resolution. For the calorimeter in barrel and ion-Endcap, where the energy resolution is not a critical factor and the e/π identification performance will be a challenge, a Shashlik-style sampling calorimeter [4–6] is adopted as a compromise between the performance and the budget constraints.

The geometry of the ECAL is illustrated in Fig. 4. The inner radius of the ECAL barrel is designed to be 0.9 m. Due to the differing measurement requirements between the electron and ion endcaps, the angular coverage in the barrel region is asymmetric, resulting in different barrel lengths on the electron and ion sides. The front planes of the e-Endcap and ion-Endcap are positioned at distances of 1.8 m and 3.5 m from the interaction point (IP), respectively. All ECAL modules are designed with a projective geometry and are oriented approximately toward the IP.

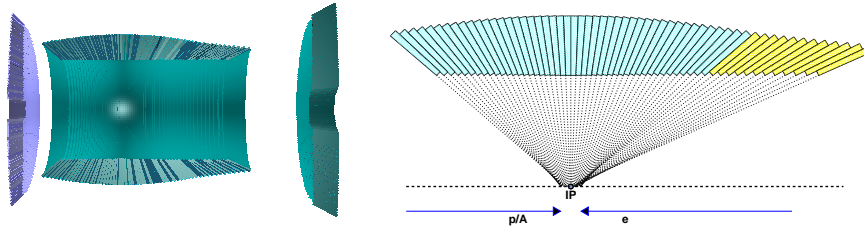


Figure 4. Overall design of the electromagnetic calorimeter (left), where the CsI crystal modules are shown in purple and the Shashlik modules in blue. Barrel module arrangement in a single row (right). Modules of the same color (blue or yellow) have identical geometry.

Parameter	e-Endcap	Barrel	ion-Endcap
Material	pCsI	Shashlik	
Distance to IP [m]	1.8	0.9 (radius)	3
η acceptance	[-3, -1]	[-1, 1.5]	[1.5, 3]
Inner radius [cm]	18	90	30
Outer radius [cm]	153	150	145
Length [cm]	30 + 5 (readout)	49 + 11 (readout)	
Radiation length [X_0]	16	16	
Molière radius [cm]	3.5	5.02	
Front size [cm ²]	4×4	4×4	
Rear size [cm ²] (max)	4.67×4.67	5.8×6.1	4.6×4.6
N layers	-	240	
Scintillator thickness [mm]	-	1.5	
Lead thickness [mm]	-	0.35	
Reflector thickness [mm]	-	0.075	
Sampling ratio	-	0.33	
N fibers (front)	-	16	
Photon detector	APD or SiPM	6×6 mm ² SiPM	
Total modules	~3900	~8000	~3900

Table 1. The summary table of calorimeter design.

It should be noted that these geometric parameters are not yet finalized, as they remain highly dependent on the dimensions of the inner detector systems. A summary of the key parameters of the current ECAL design is provided in Table 1.

In addition to the geometrical requirements, the expected energy coverage of the calorimeter is determined by the underlying event energy distributions, as previously shown in Fig. 2. For the e-Endcap, the crystals are designed to measure energy deposits from 10 MeV up to 4 GeV. For the Shashlik calorimeters, the minimum detectable energy is about 25 MeV, while the maximum energy reaches about 10 GeV in the barrel region and up to 15 GeV in the ion-Endcap. These ranges define the required dynamic measurement capability of the detector and impose corresponding constraints on the detector design, including sensor response and signal readout.

2.1 CsI Module Design

For the R&D of the e-Endcap, two types of homogeneous Cesium Iodide (CsI) crystal materials are under consideration: pure CsI (pCsI) [7] and thallium-doped CsI (CsI (Tl)) [8]. Both materials offer comparable costs and exhibit excellent intrinsic energy resolution, typically around $2\%/\sqrt{E(\text{GeV})}$. The main properties and differences between pCsI and CsI (Tl) are summarized in Table 2.

The light yield of CsI (Tl) is approximately ten times higher than that of pCsI. However, simulation studies indicate that this increased light yield does not significantly improve the energy resolution, as the statistical uncertainty from photon counting is already sufficiently small. One drawback of CsI (Tl) is its long scintillation decay time, which could potentially lead to event pile-up, especially under high-rate conditions. Another limitation is its relatively short attenuation

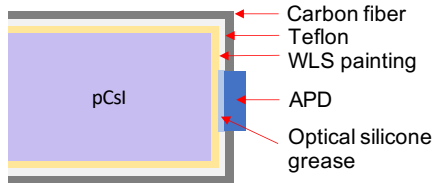
Table 2. The property comparison of pCsI and CsI (Tl) [9].

Parameters	pCsI	CsI (Tl)
Density [g/cm ³]	4.51	
Radiation length X_0 [cm]	1.86	
Molière radius [cm]	3.57	
Refractive index (peak)	1.95	1.79
Hygroscopicity	Slightly	Slightly
Emission spectrum peak [nm]	310	550
light yield rel. to NaI [%]	5.6	45
Decay time [ns]	35	1300
Absorption length of peak [cm]	100	30
Preferred photon detector	APD	PD

length, measured to be about 30 cm for photons with a wavelength of 550 nm [10], which can cause variations in photon collection efficiency depending on the depth of energy deposition within the crystal.

In contrast, pCsI provides superior timing performance owing to its much shorter scintillation decay time. However, its emission peak at 310 nm lies in the ultraviolet region, and its relatively low light yield necessitates the use of photodetectors with high quantum efficiency in the UV range. Taking these factors and the demand for precise timing capability into account, pCsI has been selected as the crystal material for the e-Endcap.

The pCsI modules in the e-Endcap are designed with a projective trapezoidal geometry, featuring a total longitudinal length of 30 cm, equivalent to approximately $16X_0$ radiation lengths. Each module has a lateral dimension of 4×4 cm² at the front face, expanding to a maximum of about 4.7×4.7 cm² at the rear face. Scintillation photons are collected by two large-area, UV-sensitive avalanche photodiodes (APDs), model Hamamatsu S8664-1010 [11], which offer a large dynamic range and relatively high quantum efficiency in the ultraviolet region. A schematic of the pCsI module design is shown in Fig. 5.

**Figure 5.** The pCsI module design.

The light yield is enhanced by coating the surface of the pCsI crystal with the wavelength-shifting (WLS) material NOL9 [12]. NOL9 converts the ultraviolet scintillation light emitted by pCsI into yellow wavelengths, where the APDs exhibit higher quantum efficiency. The crystal module is further wrapped with Teflon tape, providing high reflectivity, particularly in the ultraviolet region. Optical silicone grease is applied between the APDs and the crystal surface to eliminate any air gap, as an air layer could cause total internal reflection and reduce photon collection efficiency.

For mechanical stability and to maintain a light-tight enclosure, the entire assembly is housed within a carbon-fiber shell.

2.2 Shashlik Module Design

The Shashlik-style calorimeter is a sampling calorimeter comprising alternating layers of active and absorbing materials, with wavelength-shifting (WLS) fibers passing through each layer to collect scintillation light. It provides moderate energy resolution and has been adopted as a cost-effective solution for the ECAL calorimeters in both the barrel and ion-endcap regions. Recent beam tests have demonstrated that the Shashlik calorimeter can achieve an energy resolution of approximately $4.5\%/\sqrt{E(\text{GeV})}$ [13], which is sufficient to meet the requirements for high-energy photon measurement and e/π PID. The design parameters of the Shashlik calorimeter, including the sampling ratio, the number of layers, and the lateral cell size, can be adjusted to meet ECAL's specific performance requirements. For example, the longitudinal structure primarily affects the energy resolution, whereas the lateral dimension influences the position resolution.

In the current design, the alternating layers of the Shashlik module have been carefully optimized to balance performance requirements and engineering constraints. Based on simulation studies and experience from previous Shashlik calorimeter designs [4–6], a configuration comprising 240 layers of 1.5 mm thick plastic scintillator as the active material and 0.35 mm thick lead plates as the absorber has been selected, the design of which has a sampling ratio of 0.33, as illustrated in Fig. 6. This configuration provides a total thickness of approximately $16 X_0$, enabling effective photon detection for energies up to 15 GeV.

While simulation results indicate that increasing scintillator thickness and additional layers improve energy resolution through more complete energy deposit collection, these advantages are offset by longer module dimension and heightened light attenuation. The chosen configuration balances these opposing considerations to optimize detector performance and practical implementation.

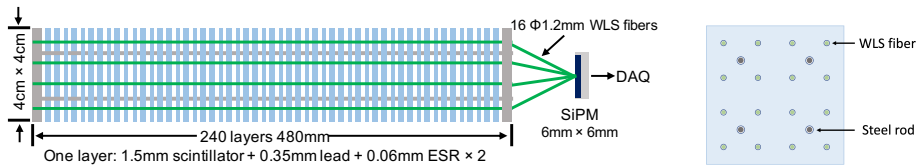


Figure 6. Longitudinal (left) and transverse (right) structural schematics of the Shashlik module.

The Shashlik module features a lateral size of $4 \times 4 \text{ cm}^2$. Each module is equipped with 16 double-cladding WLS fibers, with a diameter of 1.2 mm, which penetrate longitudinally through the holes in each layer to collect both scintillation and Cherenkov photons. The light collected by the WLS fibers is read out by a $6 \times 6 \text{ mm}^2$ SiPM mounted at one end of the module. To keep all layers firmly compressed together, four stainless-steel rods are used to apply adequate mechanical pressure.

To enhance the light yield, a $65 \mu\text{m}$ thick 3M™ ESR mirror film, with a typical reflectivity greater than 98% for visible light, is inserted between the scintillator and lead plates as a reflective layer. The ESR film is also attached to the distal end of each WLS fiber, serving as a mirror

reflector. Additionally, the outer surface of the module is coated with TiO_2 paint, which enhances light collection and ensures optical isolation of the module.

Simulation results indicate that a 1 GeV electron yields approximately 8000 photoelectrons at the SiPM readout. However, the actual light yield strongly depends on the light yield of the scintillator, the specific SiPM model employed, and the photon detection efficiency (PDE) at the chosen operating overvoltage. In practice, the overvoltage is often limited by the dynamic range of the readout electronics, which can lead to a reduced effective PDE.

The design of the Shashlik calorimeter in the barrel region faces a significant challenge: the rear end of each module is substantially larger than the front end due to the relatively long module length compared with the small barrel radius. The front face of each barrel module is positioned at a radius of 90 cm and has a lateral dimension of $4 \times 4 \text{ cm}^2$. Given a module length of 50 cm, the rear face expands to approximately 6.2 cm in width. This pronounced difference between the front and rear dimensions results in a non-uniform light collection efficiency along the module, which in turn can degrade the overall energy resolution. To mitigate this effect, additional WLS fibers are inserted at the rear end of each barrel module to enhance light collection uniformity. The resulting frustum-shaped design of the barrel Shashlik modules will be further studied and optimized in future work.

3 Simulation Results and Detector Design Optimization

To evaluate the performance of the modules, Geant4 [14] simulations were conducted using a 7×7 module array for both the pCsI and Shashlik calorimeters. This configuration is sufficient to contain the majority of the lateral energy deposition from electromagnetic showers. A uniform square particle source with the same transverse size as a single module ($4 \times 4 \text{ cm}^2$) was used as input, allowing particles to hit the full module surface and thereby accounting for the overall impact of different incident positions on the detector performance. The simulations focus on both the energy deposition in sensitive materials and the photon transmission processes within the calorimeter. The evaluation and optimization of the detector design focus on several key performance metrics, including energy resolution, position resolution, and e/π PID capability.

In the simulation of photon transmission processes, a detailed and realistic detector geometry is implemented in Geant4, including scintillation materials, reflective layers, wavelength-shifting materials (fibers and NOL9 painting), and optical sensors. Optical photon production and transport are fully simulated, covering scintillation light generation, reflection, absorption, wavelength shifting, and final photon detection. All material properties are taken from manufacturer datasheets or our experimental measurements, such as light yield, attenuation length, reflectivity, wavelength conversion efficiency, and photodetector quantum efficiency. Due to the large light yield and multiple internal reflections, the full optical simulation is computationally intensive and results in relatively low running efficiency.

A cluster reconstruction algorithm based on a neural-network and cellular-automata approach [15] is applied using the number of photoelectrons (NPE) information of individual modules. Adjacent modules with high NPE are grouped into a single cluster, while isolated modules with low energy deposits and no neighbours are discarded in the reconstruction procedure. This suppression of low-energy isolated hits reduces noise contributions but may introduce a small degradation in the

energy resolution. This clustering algorithm is also employed in the π^0 reconstruction to identify two-photon candidates.

3.1 Energy Reconstruction and Resolution

The energy resolution of both the pCsI and Shashlik calorimeters at a fixed incident energy is obtained by fitting the energy deposition spectrum with a Gaussian function. However, for the pCsI crystal module, the energy deposition does not follow a purely Gaussian distribution due to the presence of asymmetric low-energy tails caused by energy leakage or photons escaping. Instead, the distribution is well described by the Crystal Ball function [16], which combines a Gaussian core with a power-law low-end tail. For the pCsI crystal, the energy resolution is approximated by the full width at half maximum (FWHM) divided by 2.35.

The energy resolution as a function of incident energy is fitted using a function with the electronic noise term ignored for the simulations [17]:

$$\frac{\sigma_E}{E} = \frac{a}{\sqrt{E(\text{GeV})}} \oplus c \quad (3.1)$$

where a is the stochastic term, which dominates the energy resolution at low energies, and c is the constant term, mainly arising from shower leakage (both lateral and longitudinal) within the finite 7×7 array, as well as non-uniform light collection among modules in the NPE-based results. The symbol \oplus denotes a quadratic sum of the two components.

The simulated energy resolution results for both electrons and photons are shown in Fig. 7, illustrating three stages of evaluation: the intrinsic energy deposition (Edep), the NPE statistics, and NPE statistics with applying the cluster reconstruction algorithm. The pCsI crystal calorimeter achieves an energy resolution of $1.76\%/\sqrt{E} \oplus 1.53\%$ for electrons, while the Shashlik calorimeter reaches $5\%/\sqrt{E} \oplus 4.2\%$. The photon energy resolution is slightly worse than that for electrons, primarily because photons have a smaller interaction cross section with matter, leading to a deeper shower start position and consequently a higher probability of energy leakage. For the Shashlik calorimeter, the energy resolution derived from NPE is significantly degraded compared to the Edep case, particularly in the constant term. This deterioration mainly arises from non-uniform light collection efficiency in the scintillator, especially its dependence on the transverse position of the energy deposition.

3.2 Position Reconstruction and Resolution

The hit position in the ECAL is reconstructed using a logarithmic energy-weighted centroid method [18], where the deposited energy (or NPE) in each module is used as the weight. Only modules above a certain energy threshold are included in the calculation. The reconstructed position is given by:

$$X_{re} = \frac{\sum_i w_i x_i}{\sum_i w_i}, \quad w_i = \max \left\{ 0, W_0 + \ln \left(\frac{E_i}{E_{total}} \right) \right\}, \quad (3.2)$$

where x_i (y_i) is the central coordinate of i -th module in the x (y) direction, w_i is the logarithmic weight factor, E_i and E_{total} is the energy deposit of single module and the sum of all modules, W_0

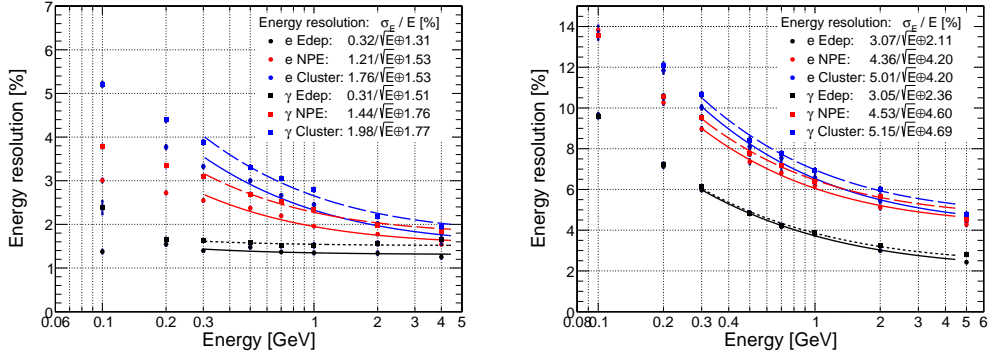


Figure 7. Simulation results of the energy resolution for electron and photon in the CsI (left) and Shashlik (right) module array.

is a constant related to energy and shower shape and used as a threshold to discard the blocks with energy deposition below $E_{total} \cdot e^{-W_0}$.

Based on simulation studies of position reconstruction, the optimized values of W_0 are found to be 4.0 for the CsI calorimeter and 3.5 for the Shashlik calorimeter. The simulated position resolution results are shown in Fig. 8. The results indicate that the impact of energy resolution on position resolution is small. For both types of calorimeters with the same transverse size, the position resolution at 1 GeV is approximately 5 mm.

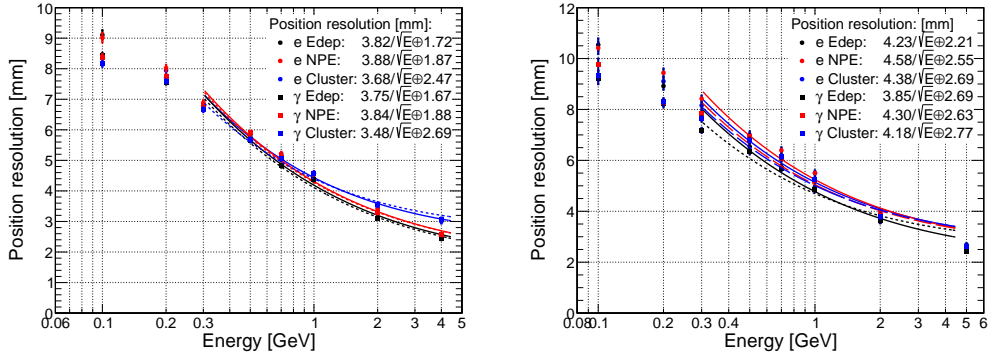


Figure 8. Simulation results of the position resolution for electrons and photons in the CsI (left) and Shashlik (right) arrays, fitted with Eq. (3.1) in the same way as the energy resolution.

3.3 Electron and Pion Identification

One of the key performance requirements of the EicC ECAL is to provide additional hadron rejection capability, particularly for distinguishing pions from electrons, while simultaneously maintaining high efficiency for electron detection. Electrons typically deposit nearly all of their energy in the calorimeter via the development of an electromagnetic shower. In contrast, high-energy hadrons primarily behave as Minimum Ionizing Particles (MIPs), depositing only a fraction of their kinematic energy in the calorimeter. This difference can be exploited using the E/p ratio, defined as the energy

deposited in the calorimeter divided by the momentum measured by the tracking detector. For this simulation, the momentum p is taken assuming ideal tracking resolution.

As shown in the left panel of Fig. 9, the E/p ratio for electrons is around the value 1, while most pions have a ratio less than 1. By applying an E/p requirement, the majority of pion contamination can be suppressed, thereby improving electron purity. However, it should be noted that a fraction of pions can undergo hadronic interactions within the calorimeter and deposit energy up to their energy. In such cases, these pions mimic the response of electrons and can contaminate the electron events, particularly when the π/e production ratio is large.

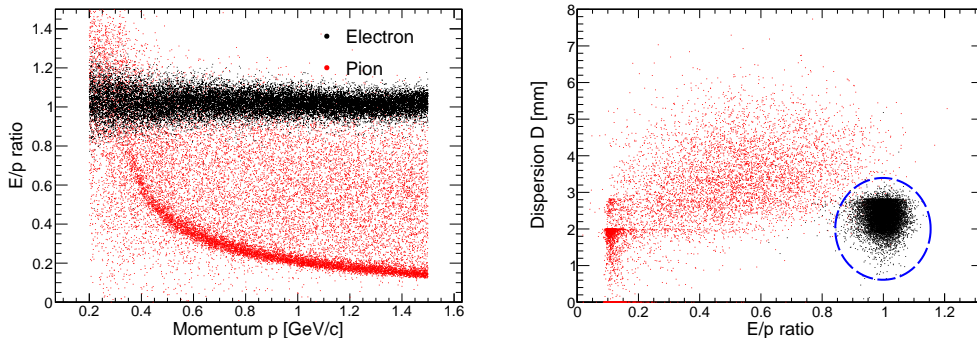


Figure 9. Simulation results of the E/p ratio for electrons and pions at various momenta (left) and the electron–pion identification method based on the shower dispersion D versus E/p at 2 GeV/c (right). A circular requirement, shown in blue, is applied to distinguish electrons from the pion background.

Additional discrimination between electrons and pions can be achieved by exploiting the difference in the spatial development of their showers. In general, hadronic showers tend to be broader and exhibit a larger lateral spread compared to the more compact electromagnetic showers induced by electrons. This characteristic can be quantified using the second moment of the hit position distribution, referred to as the shower dispersion D [18]. The total dispersion D , which accounts for both the x and y directions, is defined as:

$$D = \sqrt{D_x^2 + D_y^2} = \sqrt{\frac{\sum_i w_i (x_i - x_{re})^2}{\sum_i w_i} + \frac{\sum_i w_i (y_i - y_{re})^2}{\sum_i w_i}} \quad (3.3)$$

Similar to Eq. (3.2) for position reconstruction, x_i and y_i denote the central coordinates of each module, w_i represents the same logarithmic weight factor, and the x_{re} and y_{re} correspond to the reconstructed positions of the cluster.

Both the E/p and dispersion (D) requirements are applied to achieve high electron efficiency while ensuring effective pion rejection. The right panel of Fig. 9 shows the distribution of dispersion D versus the E/p ratio for electrons and pions in the Shashlik array. The observed structures in D reflect the distinct shower distributions: $D = 0$ corresponds to localized MIP-like pion events in a single module; $D \approx 2$ corresponds to energy sharing between two adjacent modules along a single transverse axis; and $D \approx 2.83$ ($\approx \sqrt{8}$) indicates the four-cell sharing pattern. A circular requirement is employed to optimize hadron rejection, effectively suppressing pion contamination while maintaining high electron detection efficiency. After applying the combined E/p and D

requirements, the performance reaches a pion rejection factor of about 100:1 with an electron efficiency exceeding 99%, as summarized in Table 3.

Table 3. The PID performance for 2 GeV electrons and pions after applying the selection criteria shown in the right panel of Fig. 9. Equal numbers of electrons and pions are simulated. Each column represents the PID efficiency: for example, in the first column, 99.25% of electrons are correctly identified as electrons, while 0.75% are misidentified as pions. The contamination rate is shown in the table rows, representing the fraction of misidentified particles in the final sample. For instance, in the electron sample, about $0.7/(99.25 + 0.7) \approx 0.7\%$ of pions remain as contamination after the PID selection.

Percentage[%]		Real PID	
		e	π
PID result	e	99.25	0.7
	π	0.75	99.3

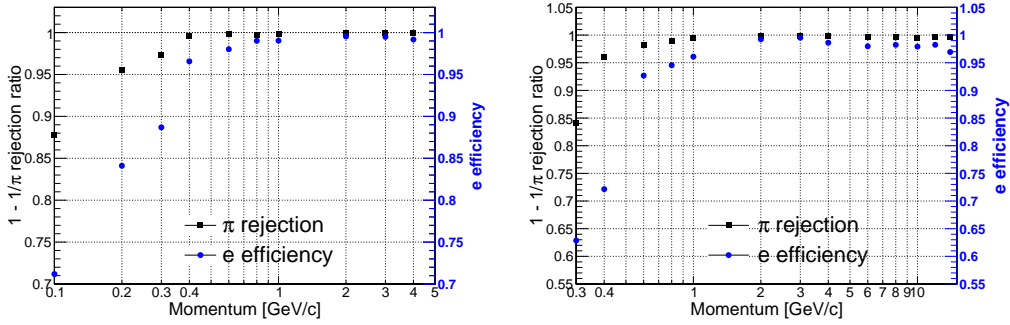


Figure 10. The pion rejection ratio and electron efficiency for different momenta of pCsI (left) and Shashlik (right) array.

The Fig.10 shows the pion rejection and electron efficiency of the pCsI and Shashlik arrays at different momenta. To better approximate realistic experimental conditions, the π/e ratio in the simulation is set to 10:1. It can be observed that both the electron efficiency and pion rejection generally improve with increasing energy. For the Shashlik calorimeter, however, the electron efficiency decreases slightly at higher energies. This is because high-energy pions increasingly exhibit electromagnetic shower-like behavior, making them more difficult to distinguish from electrons and degrading particle identification performance.

In realistic experimental conditions, as shown in Fig. 3, the π/e ratio can reach magnitudes as high as 5×10^3 , which further highlights the stringent requirements on PID performance. Several approaches can be pursued to improve the PID capability of the calorimeter system. First, further optimization of the calorimeter-based PID algorithms is necessary. Second, improvements at the detector design level, including the introduction of a preshower detector [19] and a longitudinally segmented readout scheme [20], can provide more detailed information on the early stage and longitudinal development of particle showers. Finally, effective particle identification also relies on the combined use of other PID detectors, such as Cherenkov and Time-of-Flight (TOF) systems. Such a multi-detector approach is particularly important for enhancing e/π discrimination in the low-momentum region.

3.4 Design Optimization

The calorimeter design was optimized through detailed simulations, with particular emphasis on energy resolution, which is strongly influenced by the longitudinal radiation length and sampling structure. For the pCsI module, performance can be tuned by adjusting the total crystal length, while the Shashlik module allows further flexibility by varying both the number and thickness of its alternating absorber–scintillator layers. In addition, the lateral size of the module plays a crucial role in determining position resolution, whereas the impact of energy resolution on position resolution is relatively minor. In this section, the Edep-based method was employed for both the simulation and the reconstruction in order to study the intrinsic performance of different design configurations.

As shown in Fig. 11, increasing the total radiation length improves the energy resolution, especially for high-energy electrons. However, the module length is constrained by the available space in the barrel region and by cost considerations. After evaluating different configurations, a Shashlik module with 240 layers, corresponding to about $15.8 X_0$, was chosen as a balanced solution between energy resolution and compactness. This configuration ensures adequate energy containment while maintaining manageable detector dimensions.

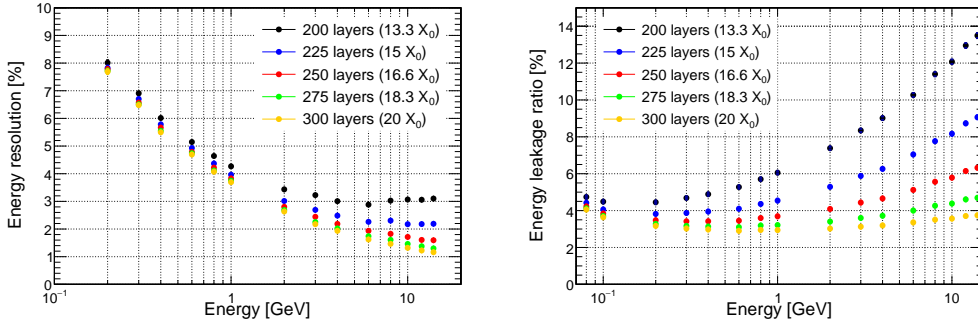


Figure 11. The energy resolution as a function of energy for different N layers (left). The energy resolution will get better with increasing layers. The energy leakage of different layers as a function of electron energy (right).

The thickness of the lead absorber layers also affects performance. Thicker absorber layers improve the energy resolution for high-energy electrons, which may benefit the ion-Endcap region where higher energies are expected. However, this comes at the cost of degraded resolution for low-energy photons, which are more sensitive to finer sampling. Therefore, the absorber thickness must be optimized according to the physics goals and energy spectrum of each detector segment, rather than adopting a single uniform design.

The lateral size of the module is another critical parameter. As indicated in Fig. 12, smaller modules yield better position resolution by offering finer spatial granularity. Nevertheless, reducing the module size increases the number of channels, which complicates the readout system and may introduce additional noise, affecting the shower reconstruction. A trade-off is therefore required between spatial resolution and system complexity.

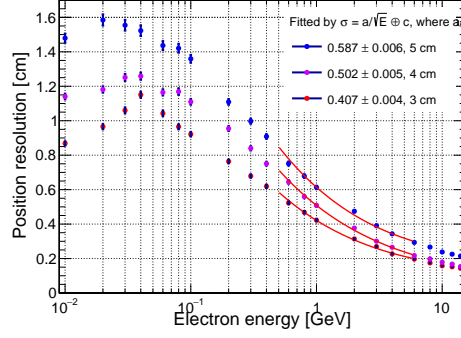


Figure 12. Position resolution as a function of energy for modules with lateral sizes of 3, 4, and 5 cm.

4 Neutral Pion Reconstruction

The reconstruction of neutral pions (π^0) is an important physics objective and a key performance benchmark of the ECAL. As a primary product of hadronization in deep inelastic scattering, π^0 measurements provide valuable information on parton fragmentation and nucleon structure, particularly in semi-inclusive and exclusive processes. In addition, the well-known π^0 invariant mass serves as a standard reference for ECAL calibration and energy resolution validation. Therefore, efficient and precise π^0 reconstruction is both a physics requirement and a crucial indicator of the overall ECAL performance.

Since π^0 decays into two photons in about 99% of cases, detecting both photons and separating those with small opening angles is crucial. The precision and efficiency of π^0 reconstruction depend on multiple factors, including energy and angular resolutions, detector acceptance, and shower separation capability. These factors reflect the combined performance of both the calorimeter and the reconstruction algorithm.

The distribution of π^0 mesons from EicC ep collisions was shown in the right panel of Fig. 2. Low-momentum π^0 events are abundant in the barrel region, while high-momentum events are concentrated in the ion-Endcap. These two regimes place different demands on detector design and reconstruction strategies.

In the π^0 rest frame, the two decay photons are emitted back-to-back with an opening angle of 180° . When the photon emission direction is perpendicular to the π^0 boost direction, the opening angle observed in the laboratory frame reaches its minimum. Assuming that the π^0 moves along the z axis, the opening angle between the two photons can be expressed as

$$\theta_{\gamma\gamma} = 2\theta = 2 \tan^{-1} \left(\frac{\sin \theta^*}{\gamma(\cos \theta^* + \beta)} \right) \quad (4.1)$$

where θ is the angle between each photon and the π^0 momentum direction in the laboratory frame after Lorentz transformation, and θ^* is the photon emission angle in the rest frame. When $\theta^* = \pi/2$, both photons are perpendicular to the π^0 flight direction, and in this case the opening angle reaches its minimum value:

$$\theta_{\gamma\gamma}^{min} = 2 \tan^{-1} \left(\frac{1}{\gamma\beta} \right) = 2 \tan^{-1} \left(\frac{m_{\pi^0}}{p_{\pi^0}} \right). \quad (4.2)$$

Fig. 13 shows the distribution of the opening angle between the two decay photons for different π^0 momenta, obtained from Geant4 simulations, which is found to be consistent with Eq. (4.2). In the relativistic limit, where the π^0 momentum is much greater than its rest mass ($p_{\pi^0} \gg m_{\pi^0}$), Eq. (4.2) can be approximated by $\theta_{\gamma\gamma} \approx 2m_{\pi^0}/p_{\pi^0}$. This approximation clearly illustrates that the opening angle between the two photons decreases rapidly with increasing energy of π^0 , leading to a higher probability of cluster overlap in the calorimeter. This effect is particularly significant in the ion-Endcap region, where high-momentum π^0 mesons are predominant. To mitigate the overlap and improve the reconstruction efficiency, the calorimeter geometry can be optimized by increasing the distance between the ion-Endcap and the interaction point and by refining the cluster reconstruction algorithms.

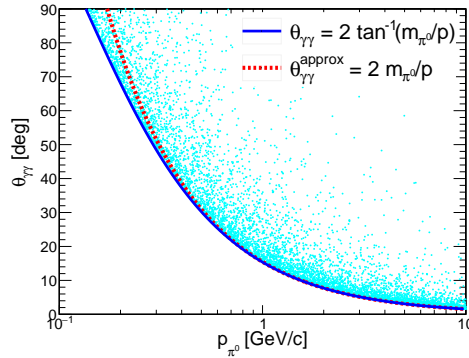


Figure 13. Angular distributions between the two decay photons from π^0 mesons with different momenta obtained from Geant4 simulation.

Simulation results using a more realistic geometry, as illustrated in the left panel of Fig. 4, indicate three main factors that can degrade the π^0 reconstruction efficiency. First, the energy of each decay photon must exceed the electronic threshold to suppress noise and ensure reliable detection. In this study, each photon cluster is required to satisfy a minimum energy threshold of 10 MeV. Second, one of the photons may escape through the beam hole or hit the detector edge, resulting in a loss of geometric acceptance. The geometric acceptance efficiency is defined as the fraction of generated π^0 events for which both decay photons fall within the ECAL acceptance, as illustrated in the left panel of Fig. 14.

Third, when the opening angle between the two photons is small, their electromagnetic showers may overlap, leading to the reconstruction of a single cluster. The reconstruction efficiency is defined as the fraction of events in which two photon clusters are reconstructed in the ECAL and their invariant mass falls within the 110–160 MeV window, relative to the number of events satisfying the geometric acceptance requirement. As shown in the right panel of Fig. 14, high-momentum π^0 mesons exhibit lower reconstruction efficiency. Improving the angular resolution, for example by increasing the distance between the detector and the IP, together with optimizing the reconstruction algorithm, can effectively mitigate this inefficiency.

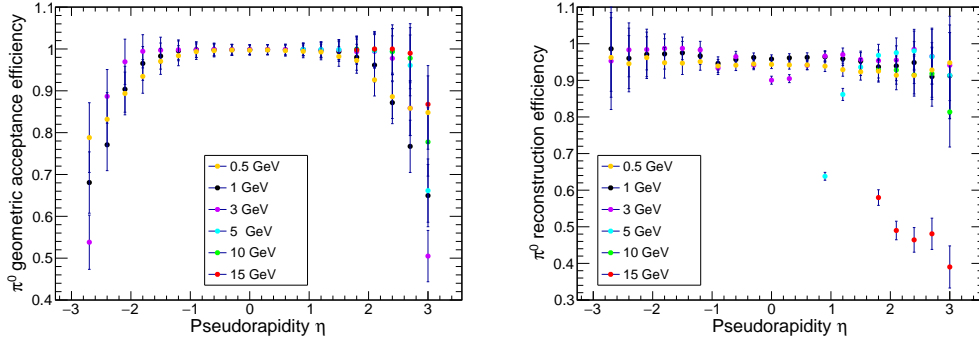


Figure 14. The π^0 geometric acceptance efficiency as a function of pseudorapidity for different momenta (left), and the π^0 reconstruction efficiency (right).

5 Conclusions

A comprehensive design and optimization study of the ECAL for the EicC has been presented, combining two complementary technologies to meet the distinct physics and geometric requirements of the detector: a pCsI crystal calorimeter in the e-Endcap and Shashlik-style sampling calorimeters in the barrel and ion-Endcap regions.

Detailed Geant4 simulations, incorporating realistic detector responses, show that the proposed configuration meets the performance targets required by the EicC physics program. The pCsI modules offer excellent energy resolution of $1.76\%/\sqrt{E(\text{GeV})} \oplus 1.53\%$, superior position resolution, and strong timing performance, benefiting from their enhanced effective light yield. The Shashlik modules, optimized in sampling structure, radiation length, and light collection uniformity, provide energy and position resolutions of $5\%/\sqrt{E(\text{GeV})} \oplus 4.2\%$ and 5 mm at 1 GeV, respectively, along with effective electron-pion separation.

These results indicate that the current ECAL design can reliably support precision measurements of electrons and photons across the full acceptance of the EicC detector. Future work will focus on detailed digitization modeling, prototype construction and validation, and advancing the ECAL toward full engineering design and construction.

Acknowledgments

This work is supported by National Key R&D Program of China under Contract No. 2023YFA1606903, CAS Pioneer Hundred Talents Program, and Postdoc Program of Department of Human Resources and Social Security of Gansu Province.

References

- [1] D. P. Anderle, V. Bertone, X. Cao et al., *Electron-ion collider in China*, [Front. Phys.](#) **16** (2021) 64701.
- [2] J. Yang et al., *High Intensity heavy ion Accelerator Facility (HIAF) in China*, [Nucl. Instr. Meth. Phys. Res. B](#) **317** (2013) 263.

- [3] T. Sjöstrand, The Pythia event generator: Past, present and future, [Comput. Phys. Commun.](#) **246** (2020) 106910.
- [4] G. Atoian, G. Britvich, S. Chernichenko et al., An improved Shashlyk calorimeter, [Nucl. Instr. Meth. Phys. Res. A](#) **584** (2008) 291.
- [5] Y. Tian, J. P. Chen, C. Feng, J. Jiao, A. Li, Y. Yu et al., Electromagnetic Calorimeter Prototype for the SoLID Project at Jefferson Lab, [Springer Proc. Phys.](#) **213** (2018) 80.
- [6] A. Semenov et al., Electromagnetic calorimeter for MPD spectrometer at NICA collider, [JINST](#) **15** (2020) C05017.
- [7] N. Atanov, V. Baranov, C. Bloise, J. Budagov, F. Cervelli, S. Ceravolo et al., Design and status of the Mu2e crystal calorimeter, [Nucl. Instr. Meth. Phys. Res. A](#) **958** (2020) 162140.
- [8] W. Li and (representing BESIII Collaboration), EM Calorimeter in BESIII Experiment, [J. Phys.: Conf. Ser.](#) **293** (2011) 012002.
- [9] R. L. Workman et al., Review of Particle Physics, [Prog. Theor. Exp. Phys.](#) **2022** (2022) 083C01.
- [10] A. Knyazev, J. Park, P. Golubev et al., Simulations of light collection in long tapered CsI(Tl) scintillators using real crystal surface data and comparisons to measurement, [Nucl. Instr. Meth. Phys. Res. A](#) **1003** (2021) 165302.
- [11] Hamamatsu, 8664-1010 Si APD Datasheet, tech. rep.
- [12] O. V. Borshchev, N. M. Surin, M. S. Skorotetcky and S. A. Ponomarenko, Highly Efficiency Wavelength Shifters: Design, Properties, and Applications, [INEOS OPEN](#) **2** (2019) 112.
- [13] Y. Li, D. Han, Y. Wang et al., Beam test results of two shashlyk ECal modules for NICA-MPD, [Nucl. Instr. Meth. Phys. Res. A](#) **958** (2020) 162833.
- [14] S. Agostinelli, J. Allison, K. Amako, J. Apostolakis, H. Araujo, P. Arce et al., Geant4—a simulation toolkit, [Nucl. Instr. Meth. Phys. Res. A](#) **506** (2003) 250.
- [15] V. Breton, H. Fonvieille, P. Grenier, C. Guicheney, J. Jousset, Y. Roblin et al., Application of neural networks and cellular automata to interpretation of calorimeter data, [Nucl. Instr. Meth. Phys. Res. A](#) **362** (1995) 478 .
- [16] M. J. Oreglia, A Study of the Reactions $\psi' \rightarrow \gamma\gamma\psi$, Ph.D. Thesis (1980) Appendix D.
- [17] C. W. Fabjan and D. Fournier, Calorimetry, in Particle Physics Reference Library: Volume 2: Detectors for Particles and Radiation, C. W. Fabjan and H. Schopper, eds., (Cham), pp. 201–280, Springer International Publishing, (2020), DOI.
- [18] T. Awes, F. Obenshain, F. Plasil et al., A simple method of shower localization and identification in laterally segmented calorimeters, [Nucl. Instr. Meth. Phys. Res. A](#) **311** (1992) 130.
- [19] K. Kawagoe, Y. Sugimoto, A. Takeuchi, T. Asakawa, J. Done, Y. Fujii et al., Performance of preshower and shower-maximum detectors with a lead/plastic-scintillator calorimeter, [Nucl. Instr. Meth. Phys. Res. A](#) **487** (2002) 275.
- [20] L. Li, Y. Li, X. Ran, Z. Deng, D. Han and Y. Wang, The study of a new longitudinal segmented shashlik electromagnetic calorimeter, [JINST](#) **20** (2025) P06033.